

Adsorption Behavior of Reducing End-Modified Cellulose Nanocrystals: A Kinetic Study Using Quartz Crystal Microbalance

Maud Chemin, Céline Moreau, Bernard Cathala and Ana Villares*

INRAE, UR BIA, F-44316, Nantes, France

*Corresponding Author: Ana Villares. Email: ana.villares@inrae.fr

Received: 5 July 2019; Accepted: 8 October 2019

Abstract: In this work, we studied the adsorption of modified cellulose nanocrystals onto solid surfaces by quartz crystal microbalance with dissipation monitoring (QCM-D). Cellulose nanocrystals obtained from tunicate (CNC) were modified at reducing end by amidation reactions. Two different functionalities were investigated: a polyamine dendrimer (CNC-NH₂), which interacts with gold surface by the amine groups; and a biotin moiety (CNC-Biot), which has a strong affinity for the protein streptavidin (SAV). QCM-D results revealed different adsorption behaviors between modified and unmodified CNCs. Hence, unmodified CNCs covered almost all the surface forming a rigid and flat layer whereas reducing end modified CNCs remained rather upright forming a hydrated and viscoelastic layer with lower surface coverage. The analysis of adsorption kinetics allowed the calculation of an apparent collision rate factor, which resulted 10-fold higher for unmodified CNCs compared to reducing end modified CNCs, therefore, demonstrating the different adsorption behavior.

Keywords: Cellulose nanocrystals; amidation; reducing-end modification; Voight model; collision rate efficiency factor; rate constant

1 Introduction

In the last decades, huge efforts have been made to develop new materials based on renewable natural resources in order to replace the toxic and/or non-biodegradable materials derived from fossil resources. Cellulose has arisen as a promising material because of its high abundance, biodegradability and non-competition with food sources [1-4]. Cellulose nanocrystals (CNCs) are produced from fibers after removal of the disordered cellulose domains by acid hydrolysis. This leads to highly crystalline nanorods excellently suited for the fabrication of advanced materials, taking advantage of their remarkable physical, mechanical, and chemical properties [2, 5]. Indeed, the presence of a high number of hydroxyl groups within their structure makes CNCs a unique platform for surface modification, generally by esterification and etherification reactions [6, 7]. Another important aspect of cellulose nanocrystals is their intrinsic chemical polarity, resulting from the parallel arrangement of cellulose chains in the cellulose I crystal. Hence, CNCs display two differentiated ends: the reducing end, which exhibits aldehyde groups, and the non-reducing end, enriched in secondary hydroxyl groups [8]. Up to present, few reports on the selective modification of cellulose nanocrystals at reducing end are described [9-13]. Recently, Lin et al. [13] introduced polyetheramine functionalities at CNCs reducing ends for leading to their temperature-driven assembly. Zoppe et al. [12] polymerized by atom transfer



This work is licensed under a Creative Commons Attribution 4.0 International License, which permits unrestricted use, distribution, and reproduction in any medium, provided the original work is properly cited.

radical polymerization (ATRP) different monomers tethered at the reducing end of cellulose nanocrystals. Furthermore, Lokanathan et al. [10, 11] introduced thiol groups at reducing ends of cellulose nanocrystals, which allowed the controlled coupling to silver nanoparticles or the chemisorption onto gold surfaces by the reducing end. In previous works, we fabricated asymmetric rods by the selective introduction of a biotin moiety at the reducing ends of cellulose nanocrystals. The modification by biotin allowed the specific assembly of several CNCs by their reducing end upon addition of the protein streptavidin [14].

The aim of the present study is to investigate the adsorption behavior of reducing end modified cellulose nanocrystals onto solid substrates. Previous studies revealed that the introduction of a chemical group at the reducing end allows specific interactions between the reducing end of modified CNCs and the surface, which results in an upright orientation of CNCs with the non-reducing end facing up [10, 14]. In this work, we give more insight into the mechanism of adsorption of cellulose nanocrystals when interactions are driven by the reducing end. The in-situ adsorption of CNCs monitored by quartz crystal microbalance with dissipation monitoring (QCM-D) was used to investigate in real time the CNCs adsorption, and the obtained results were discussed in terms of kinetic parameters of the interaction between CNCs and the surface. The analysis of adsorption kinetics allowed the elucidation of the different adsorption behaviors for the unmodified and reducing end modified CNCs, which justified the different arrangements on the surface.

2 Materials and Methods

2.1 Materials

Poly(amidoamine) with ethylenediamine core (PAMAM) dendrimer of generation 2.0 (polyamine), biotin-dPEG®7-NH₂ (Biot), streptavidin from *Streptomyces avidinii* (SAV), N-(3-dimethylaminopropyl)-N-ethylcarbodiimide hydrochloride (EDC), N-hydroxysuccinimide (NHS), sodium chlorite (NaClO₂) and potassium chloride (KCl) were purchased from Sigma-Aldrich (France) and were used without further purification. Poly (allylamine hydrochloride) (PAH) was purchased by PolySciences (Mw 120-200 000 g·mol⁻¹). Spectra/Por dialysis membrane, MWCO 12-14000 Da, was purchased from Spectrum Laboratories Inc. Water was purified by Millipore Milli-Q purification system (18.2 MΩ).

2.2 Cellulose Nanocrystals Preparation

Tunicate nanocrystals (CNC) were obtained from tunicates (*Styela clava*) collected in Quimiac beach (France), as previously described [14]. Briefly, nanocrystals were prepared by sulfuric acid hydrolysis (65%) at 40°C for 90 min under continued stirring. Then, the dispersion was cooled to 0°C, and purified by filtration (0.5 μm) and dialysis (molar mass cut off 12-14000 Da). Nanocrystals were finally re-dispersed in Milli-Q water at 6 g·L⁻¹.

The quantity of charges on the CNC surface was measured by conductometric titration with a 0.001 M NaOH solution by a TIM900 titration manager and a CDM230 conductimeter equipped with a CDC749 conductivity cell.

2.3 Functionalization at the Reducing End of CNCs

CNCs were functionalized at reducing ends in aqueous media, following the procedure previously described with minor modifications [11]. The aldehyde groups on the reducing ends of CNCs (345 mg) were oxidized to carboxyl groups by the addition of 8.7 mmol of NaClO₂, and the pH was adjusted to 3.5 using acetic acid (1 M), followed by stirring for 20 h at room temperature. The reaction mixture was subsequently centrifuged at 20000g for 30 min and, after redispersion, dialyzed against Milli-Q water to remove excess reactants and side products.

A 2 g·L⁻¹ suspension of CNC-COOH (6 mL, pH 7) was degassed by bubbling nitrogen for 20 min, and 0.7 μmol of NHS were added, followed by 7 μmol of EDC, and the pH was adjusted to 6.5 by the addition of several droplets of HCl 0.1 M. Appropriate amounts of KCl were added such that the final suspension was

0.3 M. Then, 0.2 μmol of polyamine dendrimer or biotin-dPEG®7-NH₂ were added and the pH of the reaction mixture was adjusted to 9.2 with KOH 0.1 M. The reaction was incubated under stirring at room temperature overnight. Functionalized CNCs were purified by centrifugation (20000g, 60 min, 20°C) and then dialyzed (molar mass cut off 12-14000 Da) against Milli-Q water for 15 days.

2.4 Preparation of Surfaces

SAV surfaces were prepared by adsorbing 100 μL of streptavidin at 0.5 $\text{g}\cdot\text{L}^{-1}$ on QCM-D gold electrodes for 30 min. The film was rinsed with deionized water and dried under a nitrogen stream. PAH surfaces were prepared by spin-coating. 1 mL of a PAH solution (1 $\text{g}\cdot\text{L}^{-1}$) was poured onto the QCM-D gold electrode and, after 5 min of adsorption, the substrate was spun at 3600 rpm for 60 s. The film was then rinsed with 1 mL of deionized water and spun.

2.5 Quartz Crystal Microbalance with Dissipation Monitoring (QCM-D)

The QCM-D measurements were performed with a Q-Sense E4 instrument (AB, Sweden) using a piezoelectric AT-cut quartz crystal coated with gold electrodes on each side (QSX301, Q-Sense). All measurements were carried out at 20°C using the QCM flow cell modules. Frequency ($\Delta f_n/n$) and dissipation (ΔD_n) changes were simultaneously registered at 5 MHz fundamental resonance frequency and its several overtones as a function of time. Any material adsorbed on the crystal surface induces a decrease of the resonance frequency (Δf). If the adsorbed mass is evenly distributed, rigidly attached and small compared to the mass of the crystal, Δf is directly proportional to the adsorbed mass per surface unit ($\Delta\Gamma$) using the Sauerbrey's equation [15]:

$$\Delta\Gamma = -C \frac{\Delta f}{n} \quad (1)$$

where C is the constant for the mass sensitivity of the quartz crystal (0.177 $\text{mg}\cdot\text{m}^{-2}\cdot\text{Hz}^{-1}$ at $f_0 = 5$ MHz) and n is the overtone number.

If the adsorbed film is rigid, the bulk water exerts a mass load and a viscous (damping) effect and the Sauerbrey's equation can be used for calculating the adsorbed mass. Nevertheless, for a dissipative film, the effects on frequency and dissipation from the bulk water are different. In that case, both the viscoelastic behavior of the adsorbed film and the effects from the bulk liquid must be taken into account by the Voight-based model [16]. The adsorbed layer is represented as a homogeneous film on the sensor surface using three unknown parameters: thickness (d_f), shear elasticity (μ_f), and shear viscosity (η_f); and the assumed density (ρ_f) of 1500 $\text{kg}\cdot\text{m}^{-3}$ [17]. The surrounding solution was assumed to be a semi-infinite bulk liquid ($\rho_l = 1000$ $\text{kg}\cdot\text{m}^{-3}$ and $\eta_l = 0.001$ $\text{kg}\cdot\text{m}^{-1}\cdot\text{s}^{-1}$). The adsorption curves for multiple overtones were used for estimating the adsorbed mass by the software QTools 3.1.25.604 (Q-Sense). Results are expressed as the mean of at least 3 experiments.

For QCM-D experiments, a baseline was first established by continuously flowing pure water solution or phosphate buffer (10 mM) at pH 7 for the CNC-Biot experiments on the quartz crystal surface. Then frequency and dissipation signals were off-set to zero just before injection of CNCs in a continuous mode at a flow rate of 0.1 $\text{mL}\cdot\text{min}^{-1}$. CNC dispersions (at 0.5 $\text{g}\cdot\text{L}^{-1}$) were injected into the QCM-D cell until a plateau value of frequency and dissipation signals was reached. Then, a rinsing step of the surface with water (for unmodified CNC and CNC-NH₂) or phosphate buffer (10 mM) at pH 7 (for CNC-Biot) was performed.

3 Results and Discussion

3.1 Characterization and Modification of CNC

In this work, we focused on tunicate cellulose obtained from *Styela clava*. Tunicate cellulose nanocrystals (CNC) were obtained from acid hydrolysis that removed the amorphous regions leaving the

microcrystalline segments intact. CNCs displayed nanometer scale diameters (Fig. A1), ranging from 7.5 to 13.7 nm, and an average length of 1360 ± 630 nm [14]. CNCs were negatively charged due to the presence of sulfate groups introduced during acid hydrolysis, which provided colloidal stability in water. The surface charge, measured by conductometric titration, was $0.022 \text{ mmol}\cdot\text{g}^{-1}$. CNCs were covalently functionalized at oxidized reducing ends by amidation catalyzed by the NHS-EDC system. Two different functionalities were investigated: a polyamine dendrimer, which would interact with the gold surface by the amine groups; and a biotin moiety, which has a strong affinity for the protein streptavidin (SAV). Figure 1 reviews the functionalities introduced at reducing ends of CNCs.

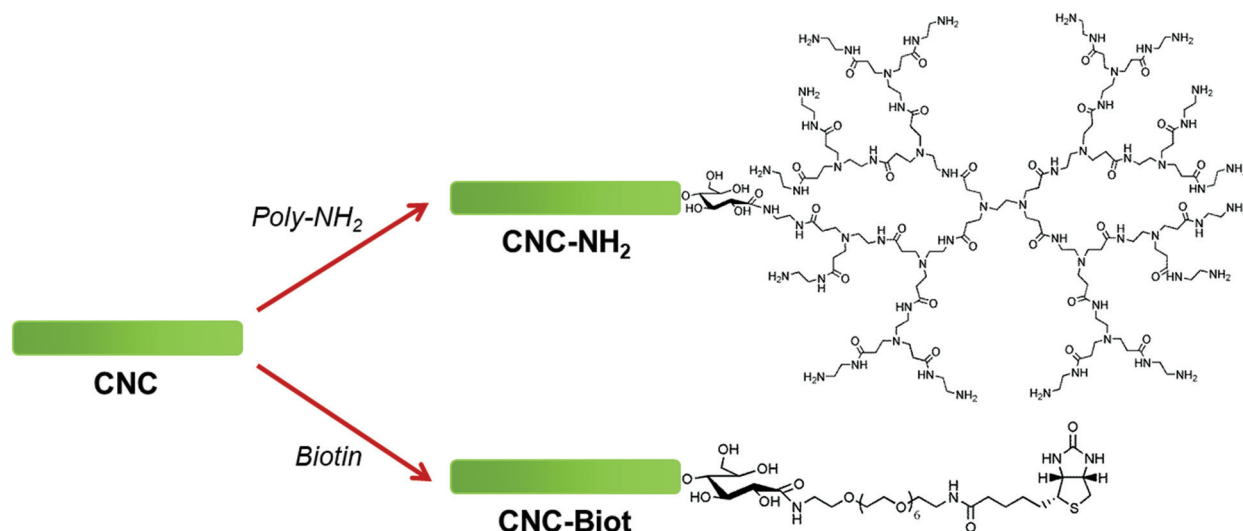


Figure 1: Schematic illustration of the structure of polyamine and biotin functionalized cellulose nanocrystals at reducing ends (CNC-NH₂ and CNC-Biot, respectively). Dimensions of CNC (green rectangles) and chemical structures are not scaled (CNC diameter is 11 ± 3 nm, hydrodynamic diameter of the polyamine is 3 nm, and that of the biotin molecule is about 0.2 nm)

3.2 Adsorption Behavior of CNC

For the adsorption studies, we investigated the behavior of three different CNCs: unmodified CNCs and two different functionalities introduced at the reducing end of the nanocrystals. Unmodified CNCs were negatively charged because of the sulfate groups introduced during acid hydrolysis; therefore, we modified gold electrodes with a layer of a cationic polyelectrolyte, the poly (allylamine hydrochloride) (PAH). The driving forces for the interaction between the negatively charged cellulose nanocrystals and PAH include electrostatic, hydrogen bonds and the entropy gain resulting from the release of counterions and water molecules [18-20]. In the case of polyamine-functionalized nanocrystals (CNC-NH₂), we took advantage of the affinity of amines for gold, similarly to the chemisorption of thiol-functionalized cellulose nanocrystals to gold surfaces described by Lokanathan et al. [10]. For biotin-functionalized nanocrystals (CNC-Biot), gold electrodes were modified by depositing a layer of streptavidin (SAV). The protein SAV has four binding sites per molecule and the streptavidin-biotin complex is one of the strongest non-covalent bindings that only dissociates in harsh conditions. Biotin appears to be specifically confined in the active site of streptavidin by hydrogen bonds and van der Waals interactions among non-polar groups [21, 22]. SAV has a near-neutral pI value [23]; therefore, to prevent unspecific adsorption of CNCs on SAV, experiments were performed in phosphate buffer at pH 7 so that SAV was negatively

charged. Thus, electrostatic repulsions between SAV and the negatively charged sulfate groups on the CNC surface discarded the adsorption of unmodified CNCs on SAV.

The adsorption of unmodified CNCs and reducing end functionalized CNCs onto solid surfaces was investigated by quartz crystal microbalance with dissipation monitoring (QCM-D). Figure 2 shows the changes in frequency ($\Delta f_n/n$) and dissipation (ΔD_n) of the three surfaces, PAH, gold and SAV, upon the injection of unmodified CNC, CNC-NH₂ and CNC-Biot, respectively. The changes of $\Delta f_n/n$ and ΔD_n signals for overtone numbers $n = 3, 5, 7, 9, 11$ and 13 are shown in the Appendix A (Figs. A2-A4).

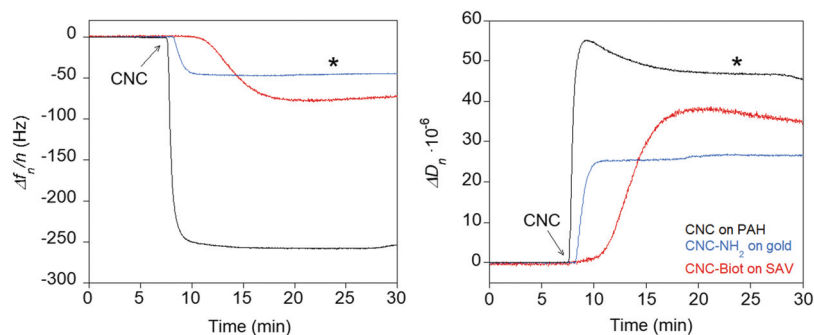


Figure 2: Normalized frequency ($\Delta f_n/n$) (left) and dissipation (ΔD_n) (right) changes for the overtone number $n = 3$ of the adsorption of CNCs as a function of time. The arrow indicates CNCs injection and the asterisk the rinsing step with water or phosphate buffer pH 7 for CNC-Biot

For both modified and unmodified CNCs, right after the injection, there was a decrease in frequency and an increase in dissipation, followed by a more gradual change until reaching the steady state. In QCM-D, the decrease in frequency is directly proportional to the adsorbed mass on the solid surface and the increase in dissipation suggests the formation of viscoelastic layers [24, 25]. As Fig. 2 shows, the injection of unmodified CNCs resulted in a rapid frequency decrease and dissipation increase, which confirmed the adsorption of CNCs on the PAH layer. The slight decrease in dissipation observed at 10 min may indicate some changes in the hydrated state of the CNCs layer on the PAH surface such that a more compacted layer was formed. In the case of modified CNCs, the frequency shifts were lower for both CNC-NH₂ and CNC-Biot whereas the dissipation reached rather high values. The differences in the frequency decrease suggested that the adsorbed mass was lower in the case of functionalized CNCs. For both modified and unmodified CNCs, the high values of dissipation suggested the adsorption of hydrated layers, which was also confirmed by the separation of overtones ($n = 3-13$, Figs. A2-A4). The stability of the layers and the irreversibility of the adsorption were assessed by rinsing with water, or phosphate buffer at pH 7 for the CNC-Biot, after complete adsorption. In all cases, rinsing did not induce significant changes in frequency or dissipation, suggesting that the nanocrystals were irreversibly attached to the surfaces. In order to discard unspecific adsorption, the interaction of unmodified CNCs with gold and SAV surfaces was also investigated by QCM-D. Upon CNC injection, nor frequency nor dissipation changed (Figs. A5 and A6), which confirmed that unmodified CNCs did not adsorb nor on gold surfaces nor on SAV layers.

In order to get more insight into the arrangement of cellulose nanocrystals onto the solid surfaces and the properties of the formed layers, the changes in ΔD_n were plotted as a function of $\Delta f_n/n$ (Fig. 3), which offers the advantage of eliminating time as an explicit parameter. The ratio between normalized frequency and dissipation shifts gives an idea of the induced energy loss per coupled unit mass. Thus, the absolute slope

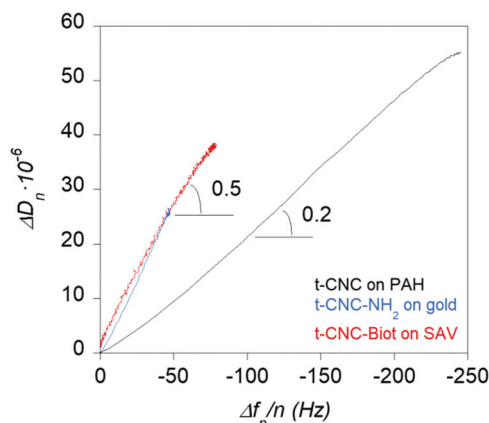


Figure 3: Change in dissipation (ΔD_n) as a function of the change in frequency ($\Delta f_n/n$) for the overtone number $n = 3$ for the adsorption of CNCs

and changes in the slope in the plots provide information about the adsorption regimes and conformation changes [26].

In all cases, dissipation increased linearly with increasing frequency, and a unique slope was obtained for both modified and unmodified CNCs. Therefore, adsorption took place as a single step process and CNCs did not undergo significant orientation changes [26]. Nevertheless, there was a stronger increase in ΔD_n for both CNC-NH₂ and CNC-Biot compared to unmodified CNCs. Table 1 reviews the frequency and dissipation values at the end of the adsorption process, and the slopes of the $\Delta D_n - \Delta f_n/n$ plots for modified and unmodified CNCs.

Table 1: Frequency ($\Delta f_n/n$) and dissipation (ΔD_n) values at the end of the adsorption process, and dissipation-to-frequency slopes obtained from the $\Delta D_n - \Delta f_n/n$ curves for the overtone $n = 3$ corresponding to the adsorption of modified and unmodified CNCs

	$\Delta f_n/n$ (Hz)	$\Delta D_n \cdot 10^{-6}$	$ \Delta D_n / \Delta f_n / n \cdot 10^{-6}$ (Hz ⁻¹)
CNC on PAH	-261.1 ± 4.2	43.9 ± 4.4	0.20 ± 0.04
CNC-NH ₂ on gold	-35.1 ± 15.3	19.6 ± 9.9	0.53 ± 0.01
CNC-Biot on SAV	-63.1 ± 92.9	31.7 ± 43.2	0.54 ± 0.13

The slope of the $\Delta D_n - \Delta f_n/n$ plot reveals at any point of the curve how dissipation changes by frequency unit allowing a comparison of the viscoelasticity characteristics of the films [24, 27]. For both modified and unmodified CNCs, the high values of dissipation ($\Delta D_n \geq 10^{-6}$) and the spreading of overtones indicated that in all cases the adsorbed layers were hydrated [28]. Nevertheless, the $\Delta D_n - \Delta f_n/n$ slopes suggested that both modified CNC-NH₂ and CNC-Biot were forming layers more dissipative and viscoelastic than unmodified CNCs. In a previous study, Lokanathan et al. [10] modified cellulose nanocrystals from Whatman filter paper at reducing ends by the introduction of thiol moieties. They studied the adsorption of both unmodified and thiol-modified CNCs on gold surfaces and they found significantly higher $\Delta D_n - \Delta f_n/n$ slopes for thiol-modified CNCs compared to unmodified CNCs. The authors ascribed the increase in slope to a more flexible conformation, where the thiol-modified CNCs chemisorbed onto the gold surface by the thiol functionality at reducing end and repelled each other electrostatically due to the presence of sulfate

groups along the nanocrystal surface. Therefore, thiol-modified CNCs adsorb on the gold surface in an upright orientation with the non-reducing end facing up. In our study, we have demonstrated that unmodified CNCs did not interact with gold or SAV surfaces (Figs. A5-A6); thus, the adsorption of CNC-NH₂ and CNC-Biot was driven by the interaction of the polyamine and biotin functionalities. These groups acted as anchoring sites at the surface and, similarly to thiol-modified CNCs [10], the presence of negatively charged sulfate groups along the nanocrystal surface could facilitate the repulsion between nanocrystals, which may result in a rather upright orientation.

3.3 Kinetic Adsorption Model

Cellulose nanocrystals can be viewed as rigid nanoparticles; therefore, the adsorption of CNCs onto solid surfaces can be analyzed by a theoretical kinetic model for particle deposition derived from the Langmuir analysis. Alince et al. [29] introduced a modified Langmuir model which is valid independently of the particle content in the system; where particles are both in excess or at less than full coverage. The kinetics of CNC deposition can be treated as a collision between the solid surface and the nanocrystals, thus, the number of particles deposited onto the surface, N_d , as a function of time, t , is given by:

$$\frac{dN_d}{dt} = \alpha_0 k_{12} S N_s \left(1 - \frac{N_d}{N_{max}}\right) \quad (2)$$

where α_0 is the collision rate efficiency factor; k_{12} is the rate constant; S is the initial number of surfaces per unit volume; N_s is the number of particles in solution; and N_{max} is the maximum number of particles that can deposit.

The fractional initial concentration, β , is the ratio between the initial number of particles in solution, N_0 , and the maximum number of particles that may deposit on the available surface, N_{max} , ($\beta = N_0/N_{max}$); and the fractional surface coverage, θ , can be defined as $\theta = N_d/N_{max}$. The kinetics of the adsorption of nanoparticles onto solid surfaces can be therefore described by the following expression [29]:

$$\frac{d\theta}{dt} = \alpha_0 k_{12} S (\beta - \theta)(1 - \theta) \quad (3)$$

In the case of CNCs, as they are rigid rod-like nanoparticles, the surface coverage may not be homogeneous, and therefore, the values of θ can differ from the unity at the steady state. Considering this assumption, the expression of the fractional surface coverage as a function of time for CNCs is:

$$\theta = \frac{1 - e^{-\alpha_0 k_{12} S \left(1 - \frac{\beta}{\theta_e}\right) t}}{\frac{1}{\theta_e} - \left(\frac{1}{\beta}\right) e^{-\alpha_0 k_{12} S \left(1 - \frac{\beta}{\theta_e}\right) t}} \quad (4)$$

where θ_e is the equilibrium fractional surface coverage at the end of the adsorption process.

This expression allows the calculation of the collision rate efficiency factor for the modified and unmodified CNCs. The values of frequency and dissipation obtained by QCM-D were transformed onto surface coverage by using the Voight's model. For the purpose of comparison, we also used the Sauerbrey's expression (Eq. (1)) for calculating the surface coverage. In all cases, the adsorbed masses calculated by the Voight's model were higher than those calculated by the Sauerbrey's equation (Fig. A7). The high values of dissipation and the high slopes from the $\Delta D_n - \Delta f_n/n$ plot indicated that the adsorbed layers were dissipative; therefore, we used the Voight's model to evaluate the fractional surface coverage.

The experimental fractional coverage values as a function of time and the theoretical curves calculated by the best fit of the kinetic model for unmodified CNC, CNC-Biot and CNC-NH₂ are shown in Fig. 4.

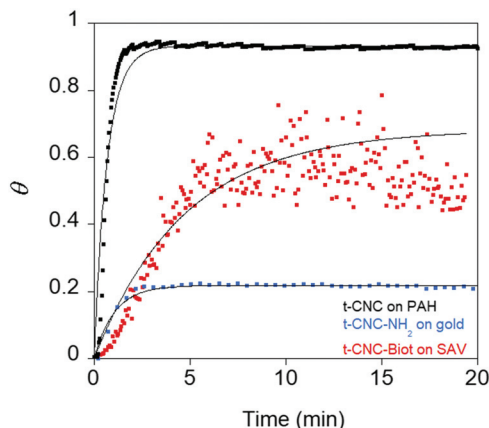


Figure 4: Fractional surface coverage for CNCs as a function of time calculated from the Voight-based model. The squares correspond to experimental data fitted by the Voight's model and the solid lines represent the fit to Eq. (4)

As the kinetic model is expressed as relative variables, i.e. θ is the ratio between the adsorbed mass and the maximum adsorbed mass, the kinetic parameters were similar by using both Sauerbrey's or Voight's models (Fig. A8 and Tab. A1). From the Fig. 4, one can see that there is a good fit between the theoretical prediction (Eq. (4)) and the measured data for all the CNCs studied. The model allowed the calculation of $\alpha_0 k_{12} S$ and the equilibrium fractional surface coverage, θ_e , for the modified and unmodified CNCs (Tab. 2).

Table 2: Values of $\alpha_0 k_{12} S$ and equilibrium fractional surface coverage, θ_e , corresponding to the adsorption of CNCs

	$\alpha_0 k_{12} S$ (min ⁻¹)	θ_e
CNC on PAH	0.113 ± 0.024	0.97 ± 0.05
CNC-NH ₂ on gold	0.014 ± 0.002	0.13 ± 0.06
CNC-Biot on SAV	0.016 ± 0.003	0.34 ± 0.45

The values of $\alpha_0 k_{12} S$ comprise the collision rate efficiency factor, the rate constant and the initial number of surfaces per unit volume. Unmodified CNCs were negatively charged with the charge uniformly distributed along the whole surface of the nanocrystal; therefore, the probability that the sulfate groups find the polycationic surface increases. When CNCs were modified at their reducing end, the collision factor decreased significantly (10-fold), and the values were independent on the chemical modification, polyamine or biotin. The values of $\alpha_0 k_{12} S$ reflected the probability of the nanocrystal to have the proper orientation to adsorb. Hence, as the functionality was selectively introduced at the reducing end of nanocrystals, their orientation should be rather perpendicular with the reducing end close enough to the surface to interact. Interestingly, the nature of the interactions did not influence the collision factor value since CNC-Biot adsorb on the SAV surface by specific protein-ligand interactions whereas CNC-NH₂ chemisorb on the gold surface. In all cases, the values of $\alpha_0 k_{12} S$ were significantly

lower than those previously obtained for the adsorption of clays on cellulose fibers (between 0.32 and 0.40 min^{-1}) [29]. In that study, the authors investigated the adsorption of clay nanoparticles on oppositely charged fibers in a dispersed medium. The authors observed that the values of $\alpha_0 k_{12} S$ decreased when the negative clay was adsorbed on positively charged fibers compared to cationic clay on neutral fibers. In our study, we studied solid surfaces, gold or macromolecules deposited on the QCM-D substrates; therefore, the lower values of $\alpha_0 k_{12} S$ might be ascribed to different availability of adsorption sites in the confined surfaces compared to dispersed media.

Concerning the equilibrium fractional surface coverage, θ_e , the adsorption of unmodified CNCs on the PAH surface showed an almost completely covered surface (97%) whereas in the case of CNC-NH₂ and CNC-Biot the surface was covered at 13% and 34%, respectively. From the differences in the chemical structure, a different mechanism of adsorption was expected for each CNC. In the case of unmodified CNCs, their negatively charged surface allowed the interaction with the polycationic layer (PAH) all along the nanocrystal. Therefore, unmodified CNCs could be adsorbed in a flat orientation driven by hydrogen bonds and electrostatic interactions of sulfate groups along the whole surface that results in a high surface coverage. In the contrary, CNC-NH₂ has 15 amino groups at reducing end that may favor the chemisorption on the gold surface; and CNC-Biot has biotin functionality at reducing end that specifically binds to the SAV surface by hydrogen bonds and van der Waals interactions. For both CNC-NH₂ and CNC-Biot the lower surface coverage compared to unmodified CNCs might be due to steric hindrance of the nanocrystal structure. Modified CNCs interact with the surface by their reducing end, and the whole nanocrystal has some degree of freedom similarly to a hairy surface. The differences between CNC-NH₂ and CNC-Biot might therefore arise from the nature and size of the anchoring group at the reducing end. Hence, in the case of CNC-Biot, the specific interaction with the SAV surface would result in a rather perpendicular orientation of nanocrystals. In contrast, the larger size of the polyamine of CNC-NH₂ may result in a less upright orientation. When the 5th generation PAMAM is introduced at the ends of nanocrystalline cellulose, Tavakolian et al. [30] described an association between the polyamine groups that connect cellulose nanorods by their ends. Therefore, in the case of CNC-NH₂, the polyamine might favor the assembly of several nanocrystals, which could be adsorbed as microtraps where steric hindrance could prevent more nanocrystals to deposit on the surface. Figure 5 shows a schematic description of the different arrangement of CNCs onto the solid surfaces.

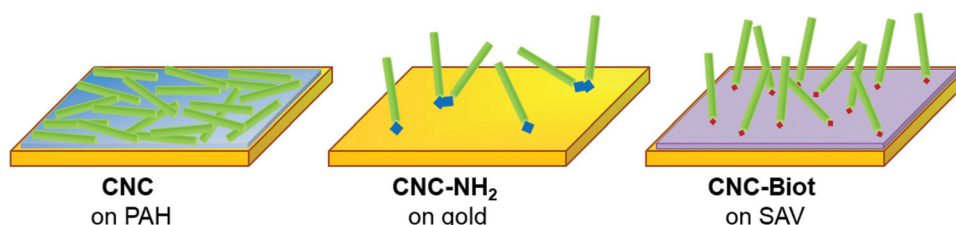


Figure 5: Schematic description of the arrangement of unmodified CNC, CNC-NH₂ and CNC-Biot, onto PAH, gold and SAV surfaces, respectively

4 Conclusions

This work gives more insight into the adsorption of nanoparticles onto solid surfaces. Results demonstrate that the presence of the functionality at the reducing end of CNCs modifies significantly the adsorption behavior of the nanocrystals. The number and distribution of anchoring groups along the nanocrystals do not only influence significantly the adsorbed amount but also the arrangement of nanocrystals on the surface. Hence, the presence of functionality at the reducing end of cellulose

nanocrystals allows their adsorption in a rather upright orientation, which results in a hairy and hydrated layer, compared to the rigid and flatly adsorbed unmodified CNCs. Moreover, the nature/size of the functional group allows tuning the surface coverage. This work opens new routes for the modification of surfaces by cellulose nanocrystals since we have demonstrated that we can control the number of adsorbed nanocrystals and their arrangement by topochemical modifications.

Acknowledgement: French National Research Agency (Project Cellmach, ANR-17-CE07-0010-01) and Region Pays de la Loire (Project Nanomach, Etoiles Montantes 2017-10691).

Conflicts of Interest: The authors declare that they have no conflicts of interest to report regarding the present study.

References

1. Klemm, D., Cranston, E. D., Fischer, D., Gama, M., Kedzior, S. A., Kralisch, D. et al. (2018). Nanocellulose as a natural source for groundbreaking applications in materials science: Today's state. *Materials Today*, *21*(7), 720–748. DOI 10.1016/j.mattod.2018.02.001.
2. Kontturi, E., Laaksonen, P., Linder, M. B., Nonappa, Gröschel, AH., Rojas, O. J. et al. (2018). Advanced materials through assembly of nanocelluloses. *Advanced Materials*, *30*(24), 1703779. DOI 10.1002/adma.201703779.
3. Berglund, L. A., Burgert, I. (2018). Bioinspired wood nanotechnology for functional materials. *Advanced Materials*, *30*(19), 1704285. DOI 10.1002/adma.201704285.
4. Keplinger, T., Wang, X. Q., Burgert, I. (2019). Nanofibrillated cellulose composites and wood derived scaffolds for functional materials. *Journal of Materials Chemistry A*, *7*(7), 2981–2992. DOI 10.1039/C8TA10711D.
5. Tang, J. T., Sisler, J., Grishkewich, N., Tam, K. C. (2017). Functionalization of cellulose nanocrystals for advanced applications. *Journal of Colloid and Interface Science*, *494*, 397–409. DOI 10.1016/j.jcis.2017.01.077.
6. Habibi, Y. (2014). Key advances in the chemical modification of nanocelluloses. *Chemical Society Reviews*, *43*(5), 1519–1542. DOI 10.1039/C3CS60204D.
7. Eyley, S., Thielemans, W. (2014). Surface modification of cellulose nanocrystals. *Nanoscale*, *6*(14), 7764–7779. DOI 10.1039/C4NR01756K.
8. Kim, N. H., Imai, T., Wada, M., Sugiyama, J. (2006). Molecular directionality in cellulose polymorphs. *Biomacromolecules*, *7*(1), 274–280. DOI 10.1021/bm0506391.
9. Sipahi-Saglam, E., Gelbrich, M., Gruber, E. (2003). Topochemically modified cellulose. *Cellulose*, *10*(3), 237–250. DOI 10.1023/A:1025151701985.
10. Lokanathan, A. R., Nykanen, A., Seitsonen, J., Johansson, L. S., Campbell, J., Rojas, O. J. et al. (2013). Cilia-mimetic hairy surfaces based on end-immobilized nanocellulose colloidal rods. *Biomacromolecules*, *14*(8), 2807–2813. DOI 10.1021/bm400633r.
11. Lokanathan, A. R., Lundahl, M., Rojas, O. J., Laine, J. (2014). Asymmetric cellulose nanocrystals: thiolation of reducing end groups via NHS-EDC coupling. *Cellulose*, *21*(6), 4209–4218. DOI 10.1007/s10570-014-0426-9.
12. Zoppe, J. O., Dupire, A. V. M., Lachat, T. G. G., Lemal, P., Rodriguez-Lorenzo, L., Petri-Fink, A. et al. (2017). Cellulose nanocrystals with tethered polymer chains: chemically patchy versus uniform decoration. *ACS Macro Letters*, *6*(9), 892–897. DOI 10.1021/acsmacrolett.7b00383.
13. Lin, F., Cousin, F., Putaux, J. -L., Jean, B. (2019). Temperature-controlled star-shaped cellulose nanocrystal assemblies resulting from asymmetric polymer grafting. *ACS Macro Letters*, *8*(4), 345–351. DOI 10.1021/acsmacrolett.8b01005.
14. Villares, A., Moreau, C., Cathala, B. (2018). Star-like supramolecular complexes of reducing-end-functionalized cellulose nanocrystals. *ACS Omega*, *3*(11), 16203–16211. DOI 10.1021/acsomega.8b02559.
15. Sauerbrey, G. (1959). Verwendung von Schwingquarzen zur Wägung dünner Schichten und zur Mikrowägung. *Zeitschrift für Physik*, *155*(2), 206–222. DOI 10.1007/BF01337937.

16. Voinova, M. V., Rodahl, M., Jonson, M., Kasemo, B. (1999). Viscoelastic acoustic response of layered polymer films at fluid-solid interfaces: Continuum mechanics approach. *Physica Scripta*, 59(5), 391–396. DOI 10.1238/Physica.Regular.059a00391.
17. Mwaikambo, L. Y., Ansell, M. P. (2001). The determination of porosity and cellulose content of plant fibers by density methods. *Journal of Materials Science Letters*, 20(23), 2095–2096. DOI 10.1023/A:1013703809964.
18. Jean, B., Dubreuil, F., Heux, L., Cousin, F. (2008). Structural details of cellulose nanocrystals/polyelectrolytes multilayers probed by neutron reflectivity and AFM. *Langmuir*, 24(7), 3452–3458. DOI 10.1021/la703045f.
19. Cranston, E. D., Gray, D. G. (2006). Morphological and optical characterization of polyelectrolyte multilayers incorporating nanocrystalline cellulose. *Biomacromolecules*, 7(9), 2522–2530. DOI 10.1021/bm0602886.
20. Moreau, C., Beury, N., Delorme, N., Cathala, B. (2012). Tuning the architecture of cellulose nanocrystal–poly (allylamine hydrochloride) multilayered thin films: Influence of dipping parameters. *Langmuir*, 28(28), 10425–10436. DOI 10.1021/la301293r.
21. Hyre, D. E., Le Trong, I., Merritt, E. A., Eccleston, J. F., Green, N. M., Stenkamp, R. E. et al. (2006). Cooperative hydrogen bond interactions in the streptavidin-biotin system. *Protein Science*, 15(3), 459–467. DOI 10.1110/ps.051970306.
22. Liu, F. J., Zhang, J. Z. H., Mei, Y. (2016). The origin of the cooperativity in the streptavidin-biotin system: A computational investigation through molecular dynamics simulations. *Scientific Reports*, 6(1), 27190. DOI 10.1038/srep27190.
23. Almonte, L., Lopez-Elvira, E., Baró, A. M. (2014). Surface-charge differentiation of streptavidin and avidin by atomic force microscopy-force spectroscopy. *ChemPhysChem*, 15(13), 2768–2773. DOI 10.1002/cphc.201402234.
24. Rodahl, M., Hook, F., Fredriksson, C., Keller, C. A., Krozer, A., Brzezinski, P. et al. (1997). Simultaneous frequency and dissipation factor QCM measurements of biomolecular adsorption and cell adhesion. *Faraday Discussions*, 107, 229–246. DOI 10.1039/a703137h.
25. Kanazawa, K. K., Gordon, J. G. (1985). Frequency of a quartz microbalance in contact with liquid. *Analytical Chemistry*, 57(8), 1770–1771. DOI 10.1021/ac00285a062.
26. Amirkhani, M., Volden, S., Zhu, K., Glomm, W. R., Nystroem, B. (2008). Adsorption of cellulose derivatives on flat gold surfaces and on spherical gold particles. *Journal of Colloid and Interface Science*, 328(1), 20–28. DOI 10.1016/j.jcis.2008.09.013.
27. Ahola, S., Salmi, J., Johansson, L. S., Laine, J., Oesterberg, M. (2008). Model films from native cellulose nanofibrils. Preparation, swelling, and surface interactions. *Biomacromolecules*, 9, 1273–1282.
28. Martins, G. V., Mano, J. F., Alves, N. M. (2010). Nanostructured self-assembled films containing chitosan fabricated at neutral pH. *Carbohydrate Polymers*, 80(2), 570–573. DOI 10.1016/j.carbpol.2009.10.030.
29. Alinec, B., Petlicki, J., Van de Ven, T. G. M. (1991). Kinetics of colloidal particle deposition on pulp fibers. I. Deposition of clay on fibers of opposite charge. *Colloids and Surfaces*, 59, 265–277. DOI 10.1016/0166-6622(91)80251-I.
30. Tavakolian, M., Lerner, J., Medina Tovar, F., Frances, J., van de Ven, T. G. M., Kakkar, A. (2019). Dendrimer directed assembly of dicarboxylated hairy nanocellulose. *Journal of Colloid and Interface Science*, 541, 444–453. DOI 10.1016/j.jcis.2019.01.100.

Appendix A.

1 Characterization and Modification of CNC

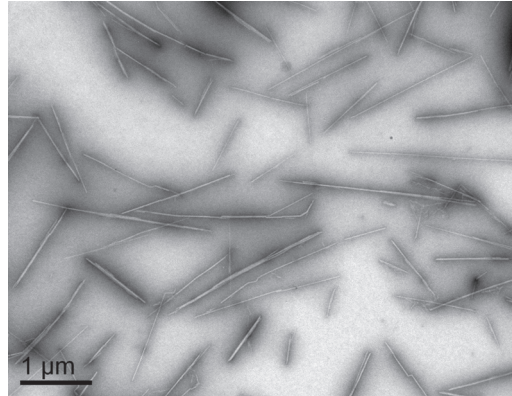


Figure A1: Transmission electron microscopy (TEM) micrograph of tunicate CNCs negatively stained with phosphotungstic acid (1%, w/v)

2 Adsorption Behavior of CNC

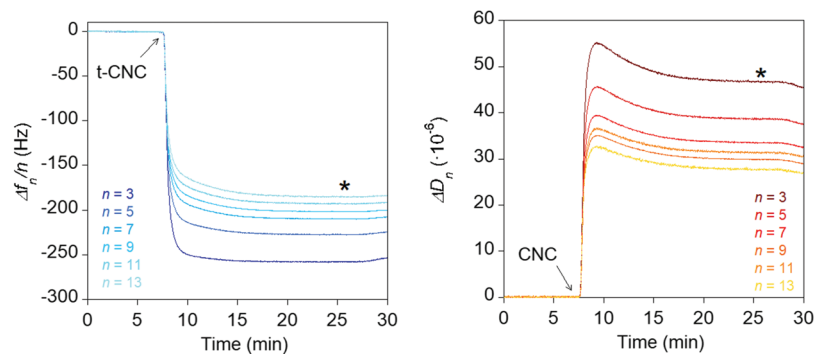


Figure A2: Normalized frequency ($\Delta f_n/n$) and dissipation (ΔD_n) changes for the overtones $n = 3, 5, 7, 9, 11$ and 13 of the adsorption of unmodified CNCs onto PAH as a function of time. The arrow indicates when CNCs are injected and the asterisk the rinsing step with water

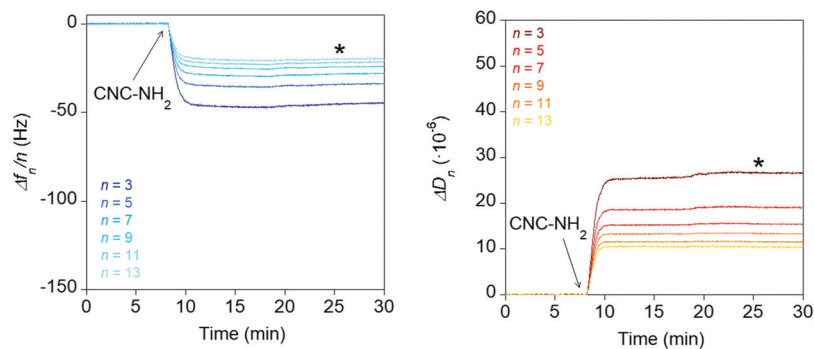


Figure A3: Normalized frequency ($\Delta f_n/n$) and dissipation (ΔD_n) changes for the overtones $n = 3, 5, 7, 9, 11$ and 13 of the adsorption of CNC-NH₂ onto gold surfaces as a function of time. The arrow indicates when CNCs are injected and the asterisk the rinsing step with water

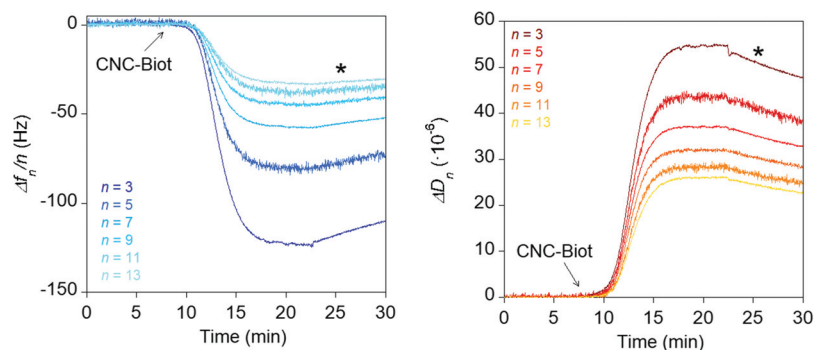


Figure A4: Normalized frequency ($\Delta f_n/n$) and dissipation (ΔD_n) changes for the overtones $n = 3, 5, 7, 9, 11$ and 13 of the adsorption of CNC-Biot onto SAV surfaces as a function of time. The arrow indicates when CNCs are injected and the asterisk the rinsing step with phosphate buffer pH 7

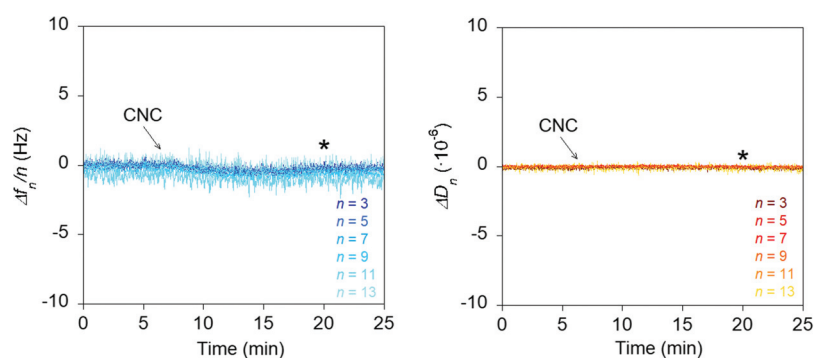


Figure A5: Normalized frequency ($\Delta f_n/n$) and dissipation (ΔD_n) changes for the overtones $n = 3, 5, 7, 9, 11$ and 13 of the adsorption of unmodified CNCs onto gold surfaces as a function of time. The arrow indicates when CNCs are injected and the asterisk the rinsing step with water

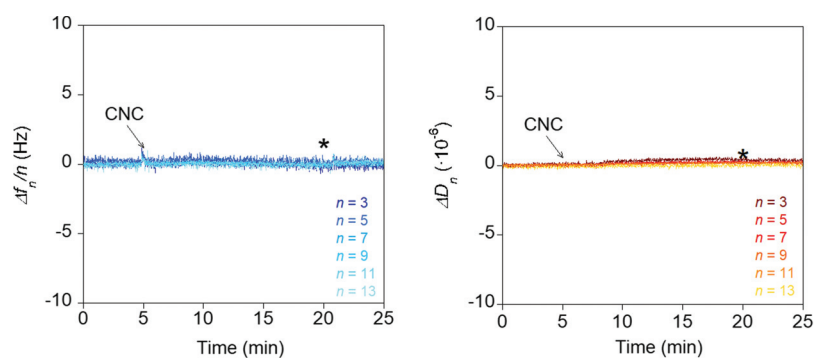


Figure A6: Normalized frequency ($\Delta f_n/n$) and dissipation (ΔD_n) changes for the overtones $n = 3, 5, 7, 9, 11$ and 13 of the adsorption of unmodified CNCs onto SAV as a function of time. The arrow indicates when CNCs are injected and the asterisk the rinsing step with phosphate buffer at pH 7

3 Kinetic Adsorption Model

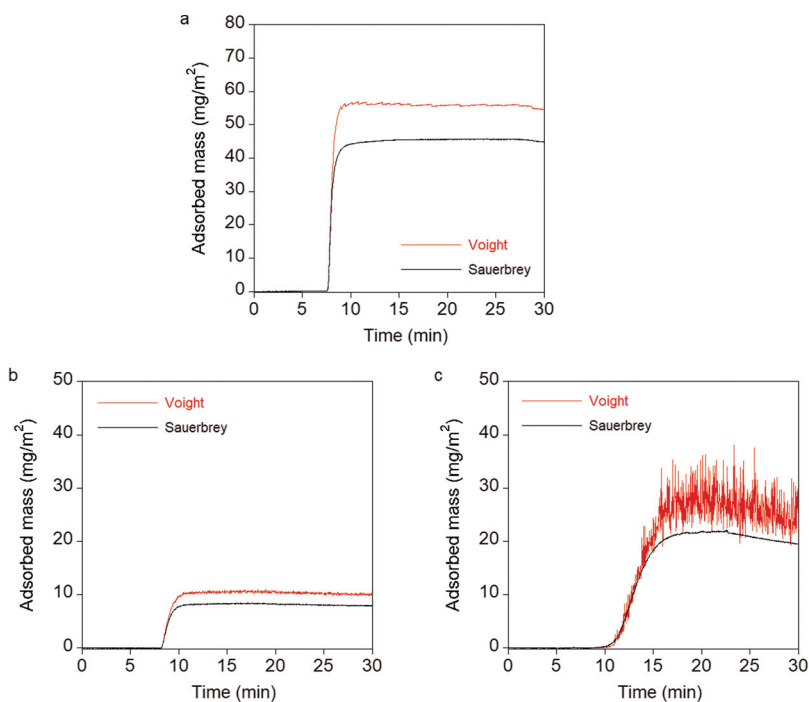


Figure A7: Calculated adsorbed masses by using the Sauerbrey's and Voight's models for CNC adsorbed on PAH (a), CNC-NH₂ adsorbed on gold (b), and CNC-Biot adsorbed on SAV (c)

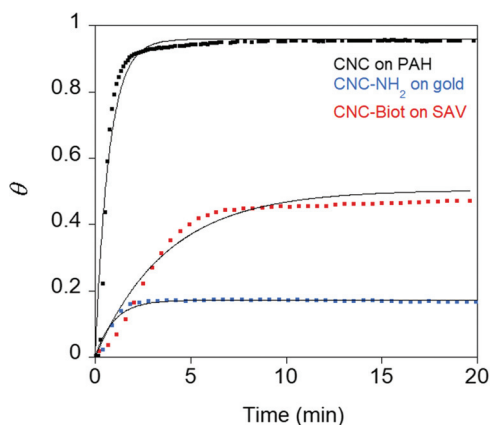


Figure A8: Fractional surface coverage for CNCs as a function of time calculated from the Sauerbrey's equation. The squares correspond to experimental data and the solid lines represent the fit to Eq. (4)

Table A1: Values of $\alpha_0 k_{12} S$ and equilibrium fractional surface coverage, θ_e , corresponding to the adsorption of CNCs calculated by using the Sauerbrey's equation to estimate the mass adsorbed

	$\alpha_0 k_{12} S$ (min^{-1})	θ_e
CNC on PAH	0.100 ± 0.005	0.96 ± 0.00
CNC-NH ₂ on gold	0.012 ± 0.002	0.13 ± 0.06
CNC-Biot on SAV	0.012 ± 0.003	0.31 ± 0.39